water

MDPI

Article

Three-Dimensional Turbulence Numerical Simulation of Flow in a Stepped Dropshaft

Yongfei Qi [1,2], Yurong Wang [1,*] and Jianmin Zhang [1,*]

[1] State Key Laboratory of Hydraulics and Mountain River Engineering, Sichuan University, Chengdu 610065, China; xjqiyongfei@163.com

[2] Department of Foundation Studies, Xinjiang Institute of Engineering, Urumqi 830023, China

* Correspondence: wangyurong@scu.edu.cn (Y.W.); zhangjianmin@scu.edu.cn (J.Z.); Tel.: +86-139-8002-5149 (Y.W.); +86-139-8187-8609 (J.Z.)

Received: 18 November 2018; Accepted: 17 December 2018; Published: 24 December 2018

Abstract: The dropshaft structure is usually applied in an urban drainage system to connect the shallow pipe network and the deep tunnel. By using the renormalization group (RNG) k~ε turbulence model with a volume of fluid method, the flow pattern and the maximum relative water depth over a stepped dropshaft with a different central angle of step were numerically investigated. The calculated results suggested that the flow in the stepped dropshaft was highly turbulent and characterized by deflection during the jet caused by the curvature of the sidewall. According to the pressure distribution on the horizontal step and the flow pattern above the step, the flow field was partitioned into the recirculating region, the wall-impinging region and the mixing region. In addition, with the increase in the central angle of step, the scope of the wall-impinging region and the mixing region increased and the scope of the recirculating region remained nearly unchanged. The maximum water depth increased with the increase in discharge. In the present work we have shown that, as the value of the central angle of step increased, the maximum water depth decreased initially and increased subsequently.

Keywords: stepped dropshaft; numerical simulation; flow region; central angle of step

1. Introduction

A dropshaft is a hydraulic structure that is installed in drainage systems and tunnel schemes to convey extreme rainfall so that it will not trigger urban flooding. The energy dissipation of a dropshaft is very notable. Studies by Rajaratnam et al., Chanson, and Camino et al. have shown that the energy dissipation rate of the dropshaft is normally more than 75% [1–4].

According to the flow features of a vertical dropshaft, the general dropshaft structure can be divided into four categories: plunge-flow dropshaft [5,6], vortex-flow dropshaft [7,8], baffle-flow dropshaft [9,10], and helicoidal-ramp dropshaft [11,12]. In recent years, vortex-flow dropshafts have become popular due to the excellent energy dissipation and air removal in the construction. The flow characteristic has been investigated by engineers and scientists through laboratory experimentation and numerical simulation. Jain and Kennedy [13] reported the application of vortex dropshafts in the Milwaukee Metropolitan Sewerage District in 1984. In 2010, Hager [14], combined with previous engineering experience, put forward a complete design plan for a vortex dropshaft. Zhao et al. [15] investigated the performance of a vortex drop structure with a relatively small height-to-diameter ratio and confirmed that the energy dissipation rate and air entrainment rate were very significant. Del Giudice and Gisonni [16] optimized the intake of a vortex drop structure in Naples and solved the problem of supercritical approach flow. Natarius [17] installed the Vortex Flow Insert (VFI) in a vortex drop which can effectively eliminate the public odor problem in that drop. Yu and Lee [18]

investigated the hydraulics of tangential vortex intake and presented the design guideline that can convey the flow steadily without being influenced by the hydraulic jump.

In order to improve energy dissipation and reduce safety hazards, an innovative design of vortex-flow structures has been developed [19]. A series of steps was deployed on the dropshaft. The flow hit each step as an impinging jet, with the energy being dissipated through jet breakup in the air, collision and swirling on the step, and increased friction between jet and sidewall [20,21]. From the perspective of safety, the steps will significantly increase the air concentration and reduce the risks of cavitation damage [22]. The features of the standing waves concerning the relative height, the location, and the extent were studied theoretically and experimentally by Wu et al. [23].

Although researchers of existing studies have gained a comprehensive understanding of this particular type of dropshaft, little is known about the intricacies of the flow and influence of central angle of step on hydraulic properties. Therefore, in order to study the effect of central angle of step on the flow pattern and maximum water depth on the sidewall, numerical investigations of a stepped dropshaft with different central angles were carried out.

2. Numerical Simulation

2.1. Volume of Fluid Method

The volume of fluid [24] model, which relies on the fact that two or three phases are not interpenetrating, provides an efficient and economical way to track the volume fraction of each of the fluids throughout the domain. Because different fluid components are solved by a single set of momentum equations, the volume fraction of unit phase is defined in order to track the free surface of each computational cell. For an air–water two-phase flow model, in each computational cell, the sum of the volume fractions of the air and water is unity. Specifically, computational cells without water have a value of zero. Full cells are assigned a value of 1 and partially filled cells have a value between 0 and 1. Therefore, the volume fraction of air or water is defined as α_a and α_w, respectively. The relationship between α_a and α_w can be given as follows:

$$\alpha_a + \alpha_w = 1 \tag{1}$$

The variables and their attributes are shared by air and water and represent volume-averaged values if the volume fraction of air and water is obtained. Therefore, at any given control volume, the variables and their attributes represent either air or water, or a mixture of them. The tracking of the interface between air and water is accomplished by the solution of the continuity equation with the following form:

$$\frac{\partial \alpha_w}{\partial t} + u_i \frac{\partial \alpha_w}{\partial x_i} = 0 \tag{2}$$

where α_w is the volume fraction of water and u_i and x_i are the velocity components and coordinates (i = 1, 2, 3), respectively.

The density ρ and molecular viscosity μ, which are the volume-fraction-averaged properties and not constants can be expressed as follows:

$$\rho = \alpha_w \rho_w + (1 - \alpha_w)\rho_a \tag{3}$$

$$\mu = \alpha_w \mu_w + (1 - \alpha_w)\mu_a \tag{4}$$

where ρ_w and ρ_a are the density of water and air and μ_w and μ_a are the molecular viscosity of water and air. By the iterating solution of the volume fraction of water α_w, ρ and μ can be calculated.

2.2. Turbulence Model

With the rapid development of computer technology, numerical methods have been applied more and more to complex flows of industrial relevance [25–30]. The most widely used approach in both academia and industry for the modeling of turbulent flows is Reynolds-averaged Navier–Stokes (RANS) methods that solve additional transport equations for turbulence and introduce the turbulence eddy viscosity to simulations to mimic the effect of turbulence. In the RANS modeling framework, two distinct turbulence models were used, namely, k~ε and k~ω. The k~ε turbulent models have historically been used in flow simulations because of the better convergence and lower memory [31,32]. Desirable results can be achieved in various contexts by the k~ω turbulent models, such as boundary layers with adverse pressure gradients and flow separation [33,34]. There are many papers which simulated the complicated hydraulic properties in stepwise and vortex shaft spillway structures using the k~ε model [35–38], yielding reliable results compared with laboratory experiments. As an improvement of the standard k~ε model, the RNG k~ε model [39] is more accurate in simulating flows with high strained rates and streamline bending [40–42], such as the swirling flow. Therefore, the RNG k~ε turbulent model was adopted to model the intricate flow in the stepped dropshaft. The computational fluid dynamics module of the ANSYS 16.0 software (ANSYS®, Canonsburg, PA, USA), Fluent [43], was utilized to investigate the flow over the stepped dropshaft. The equations of the turbulent kinetic energy, k, and its dissipation rate, ε, are as follows:

k equation:

$$\frac{\partial}{\partial t}(\rho k) + \frac{\partial}{\partial x_i}(\rho k u_i) = \frac{\partial}{\partial x_j}\left[(\mu + \frac{\mu_t}{\sigma_k})\frac{\partial k}{\partial x_j}\right] + G_k - \rho\varepsilon, \tag{5}$$

ε equation:

$$\frac{\partial}{\partial t}(\rho\varepsilon) + \frac{\partial}{\partial x_i}(\rho\varepsilon u_i) = \frac{\partial}{\partial x_j}[(\mu + \frac{\mu_t}{\sigma_\varepsilon})\frac{\partial \varepsilon}{\partial x_j}] + C_{1\varepsilon}^{*}\frac{\varepsilon}{k}G_k - C_{2\varepsilon}\rho\frac{\varepsilon^2}{k}, \tag{6}$$

$$\mu_t = \rho C_\mu \frac{k^2}{\varepsilon} \tag{7}$$

$$G_k = \mu_t(\frac{\partial u_i}{\partial x_j} + \frac{\partial u_j}{\partial x_i})\frac{\partial u_i}{\partial x_j}, \tag{8}$$

$$C_{1\varepsilon}^{*} = C_{1\varepsilon} - \frac{\eta(1-\eta/\eta_0)}{1+\beta\eta^3}, \tag{9}$$

$$\eta = \sqrt{\frac{G_k}{\rho C_{\mu\varepsilon}}}, \tag{10}$$

where ρ is the corresponding density, μ is the dynamic viscosity, μ_t is the turbulence viscosity, u_i is the velocity component in the ith direction, t is the time, G_k is the generation of turbulent energy caused by the average velocity gradient, and C_μ, $C_{1\varepsilon}$, $C_{2\varepsilon}$, β, and η_0 are empirical constants. In the RNG k~ε model, the empirical constants are given as C_μ = 0.0845, $\sigma_k = \sigma_\varepsilon$ = 0.7179, $C_{1\varepsilon}$ = 1.42, $C_{2\varepsilon}$ = 1.68, β = 0.012, and η_0 = 4.38.

2.3. Numerical Algorithm

The Pressure-Implicit with Splitting of Operators (PISO) algorithm, based on the higher degree of the approximate relation between the corrections for pressure and velocity, was applied to implicitly couple the velocity and pressure. The implicit finite volume method was used to solve the iteration. The calculated domain was divided into discrete control volumes by the unstructured grid that has a high adaptability and is self-adjusting to the complicated geometry and boundary. The detailed location of the free surface is determined by the geometric reconstruction scheme, which is accurate and applicable for general unstructured meshes in Fluent. This scheme assumes that the interface between two fluids has a linear slope within each cell, and then uses this linear shape for calculation

of the advective flux. Ultimately, the volume fraction of each cell can be calculated according to the advective flux balance of previous calculations. Refining the grid on interface between water and air is important for transient VOF calculations using the Geo-Reconstruct formulation. It was unfortunate that the water level in the dropshaft could not be measured beforehand because of the complexity and randomness in the multi-phase flow process. Consequently, in order to get the high-precision results, all the three calculated configurations were refined with total grid numbers of approximately 0.30 million, 0.46 million, and 0.65 million, respectively (the specific content will be introduced later).

The appropriate setting of time-dependent solution parameters is the magnitude guarantee of robustness and efficiency for calculation. For transient volume of fluid calculations that use the implicit scheme of VOF, the fixed times stepping method was selected. The max iterations per time step, a maximum for the number of iterations per time step, was set as 50. Since the ANSYS Fluent formulation is fully implicit, there is no stability criterion that must be met in determining the time step size. A good way to adjust the size of time step is to satisfy the ideal number of iterations per time step, which ranges from 5 to 10. To be specific, if the calculation needs only a few iterations per time step, the time step size should be increased; otherwise, it should be decreased. In this work, the range of the time step size was adjusted from 0.0001 s to 0.001 s and the iteration number was always less than 5.

2.4. Geometric Model

The calculated domain is shown in Figure 1. It has the same size as the physical model, given in the literature [19]. The numerical model consists of three main parts, namely, the inlet section, the vertical shaft section, and the outlet section. The inlet channel cross-section was rectangular, 0.15 m wide and 0.25 m deep. The length of the inlet channel was 1 m. For the vertical shaft section, the height was 1.834 m, the external radius (R) was 0.25 m, and the internal radius (r) was 0.1 m. The shaft vertical section consisted of 14 steps, which connected the inlet channel and the outlet channel. The width, b, and the height, h, of each step were 0.15 m and 0.131 m, respectively. They were numbered from S1 to S14. The central angle of step, one important structure feature of dropshaft, was defined as θ, and configurations with θ = 120°, 150°, or 180° were investigated. The dimensions of the cross-section of the outlet channel were 2 × 0.15 × 0.131 m (length × width × height).

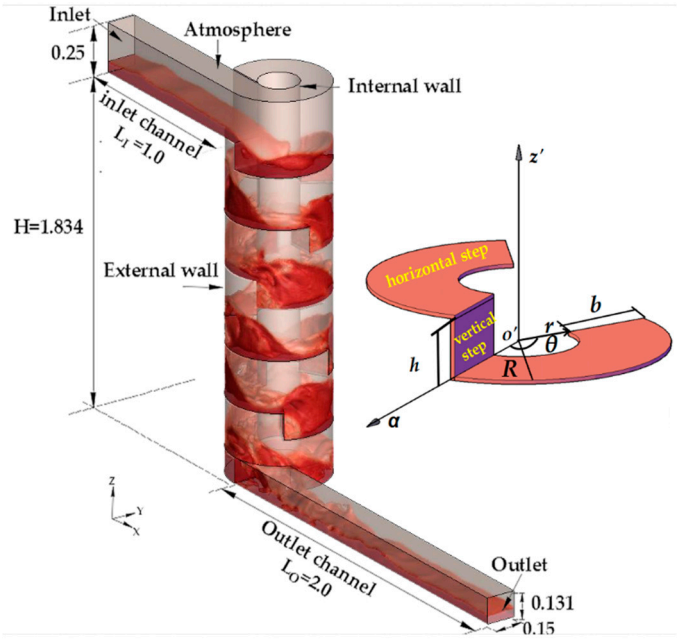

Figure 1. Computational model of the dropshaft.

In order to facilitate analysis, the cylindrical coordinate systems were established. The *z*-axis was the center axis of shaft. The relative polar coordinates were established on each step, in which the center of the circle was defined as the pole and the starting edge of the step was defined as the polar axis.

2.5. Boundary Conditions and Cases

The boundary conditions were as follows:

(1) Inlet boundary: the velocity inlet was used for the intake, which was set at 0.89–2.69 m/s;
(2) Outlet boundary: the outlet boundary was set as pressure outlet and the normal gradient of all variables was equal to 0;
(3) Free surface: the free surface of water was assumed to be the pressure inlet and the pressure value was $P = 0$; and
(4) Wall boundary: no-slip velocity boundary condition; the near-wall regions of the flow were analyzed using the method of standard wall function.

In this study, nine cases with different flow rates and different central angles of step were investigated. The calculation program is shown in Table 1. The design condition of verified cases was set up the same way as the experiment from the literature [19]: h is the step height; D is the width-radius ratio, which is the ratio of step width to external radius; i is the slope coefficient, which is spreading out from the external wall; and Fr is the Froude number of approach flow.

Table 1. Summary of the operating conditions for the simulations.

h (m)	D	θ (°)	i	Q (m^3/s)	Fr	Case
0.131	0.6	150	0.20	12.75	0.58	test1
				41.50	1.90	test2
		120	0.25	80.00	3.67	1
				48.00	2.20	2
				26.50	1.22	3
		150	0.20	80.00	3.67	4
				48.00	2.20	5
				26.50	1.22	6
		180	0.17	80.00	3.67	7
				48.00	2.20	8
				26.50	1.22	9

2.6. Verification

2.6.1. Grid Testing

It is very important to use the grid reasonably for the accuracy of calculation results. Therefore, the effects of different grid densities on the uncertainty of the calculation results were tested using the grid convergence index (GCI) [44] with grid numbers of approximately 0.65 million (grid 1), 0.46 million (grid 2), and 0.30 million (grid 3). The GCI is defined as follows:

$$\mathrm{GCI} = \frac{1.25|(\phi_1 - \phi_2)/\phi_1|}{(k_2 - k_1)^p - 1}, \tag{11}$$

in which ϕ_i represents the variable of the ith calculation, k_i represents the representative grid size for the ith calculation, and let $k_1 < k_2 < k_3$. For three-dimensional calculations, k is given by the following:

$$k = \left(\left[\frac{1}{N} \sum_{i=1}^{N} (\Delta V_i) \right] \right)^{1/3} \tag{12}$$

The order of p in Equation (11) can be estimated by the following:

$$p = \frac{1}{\ln(k_2/k_1)}\left|\ln|(\phi_3-\phi_2)/(\phi_2-\phi_1)| + \left|\ln\left(\frac{(k_2/k_1)^P - \mathrm{sgn}[(\phi_3-\phi_2)/(\phi_2-\phi_1)]}{(k_3/k_2)^P - \mathrm{sgn}[(\phi_3-\phi_2)/(\phi_2-\phi_1)]}\right)\right|\right|. \quad (13)$$

In this paper, the pressure and tangential velocity that, respectively, were written in dimensionless form as p/h and $V_\tau/V_{\tau\max}$, were variables. Figure 2b,d presents pressure and tangential velocity along a radial line that was in the *yoz* plane and paralleled to the *y*-axis (as depicted in Figure 2a) for different grid densities with Q = 41.25 m^3/s. The data obtained from grid 2 were close to the data obtained with the grid 1 and the computational efficiency decreased by 20%. In Figure 2c,e, the maximum uncertainties in pressure and tangential velocity were approximately 3.12% and 4.17%, respectively, implying that the discretization uncertainties were little in most locations. For the consideration of computational efficiency and accuracy, the grid number of 0.46 million (grid 2) was adopted in the present study.

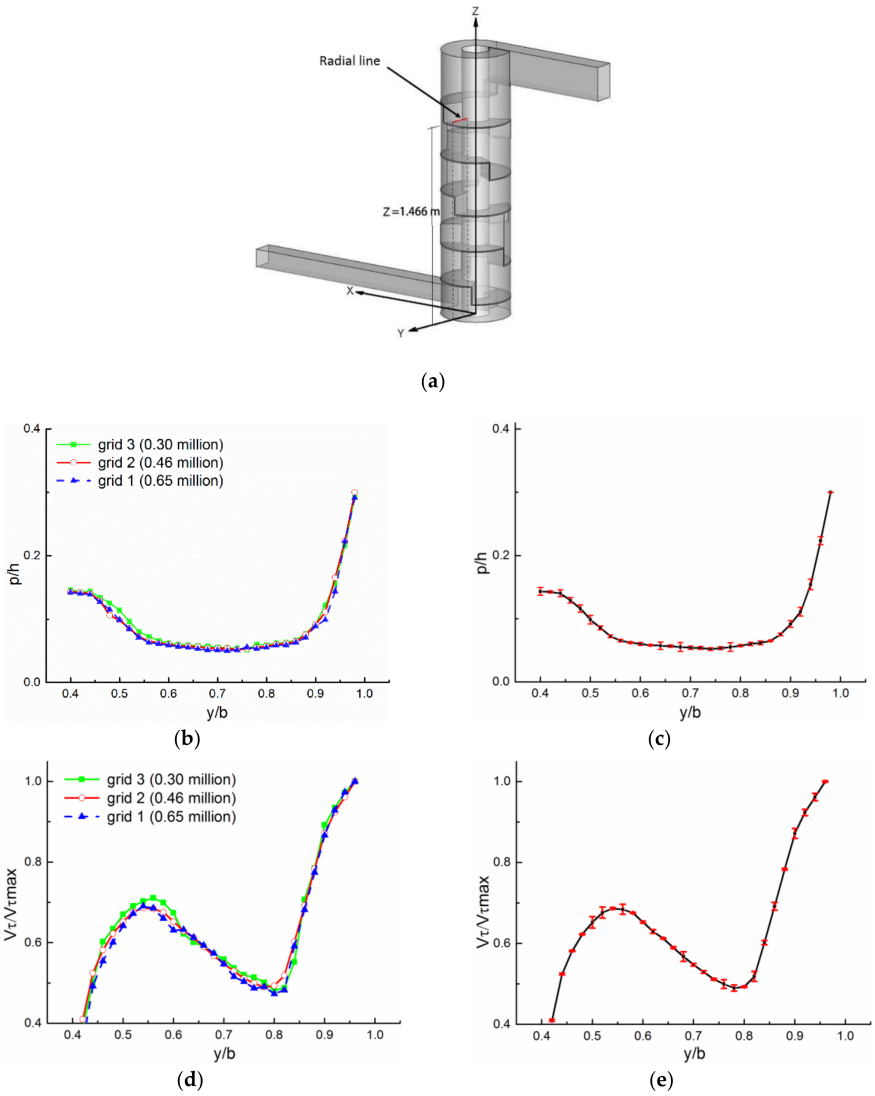

Figure 2. Grid convergence index value for different grid densities: (**a**) location of radial line; (**b**) pressure profile in models with different mesh numbers; (**c**) fine-grid solution, with discretization error bars computed using Equation (11); (**d**) tangential velocity profile in models with different mesh numbers; (**e**) fine-grid solution, with discretization error bars computed using Equation (11).

2.6.2. Model Verification

The calculated flow pattern was fairly consistent with the experimental results under different discharges, as is shown in Figure 3. When transferring from the upper steps to the lower steps, and owing to the collision between the flow and the steps, part of the flow changed direction with the mainstream travelling downstream. The flow that changed direction impacted the vertical surface of the step and formed a reflux. In addition, the cavities near the vertical step were obvious. As shown in Figure 3a,c, the main differences are as follows: (1) the recirculation zone for Q = 41.5 m^3/s was smaller than that of Q = 12.75 m^3/s; and (2) for Q = 12.75 m^3/s, there was an increase in the water level when flow entered the next step, but for Q = 41.5 m^3/s, the increase in water level occurred after the nappe flow impacted the horizontal step. As can be seen from Figure 3b,d, the simulated flow patterns were in good agreement with experimental results.

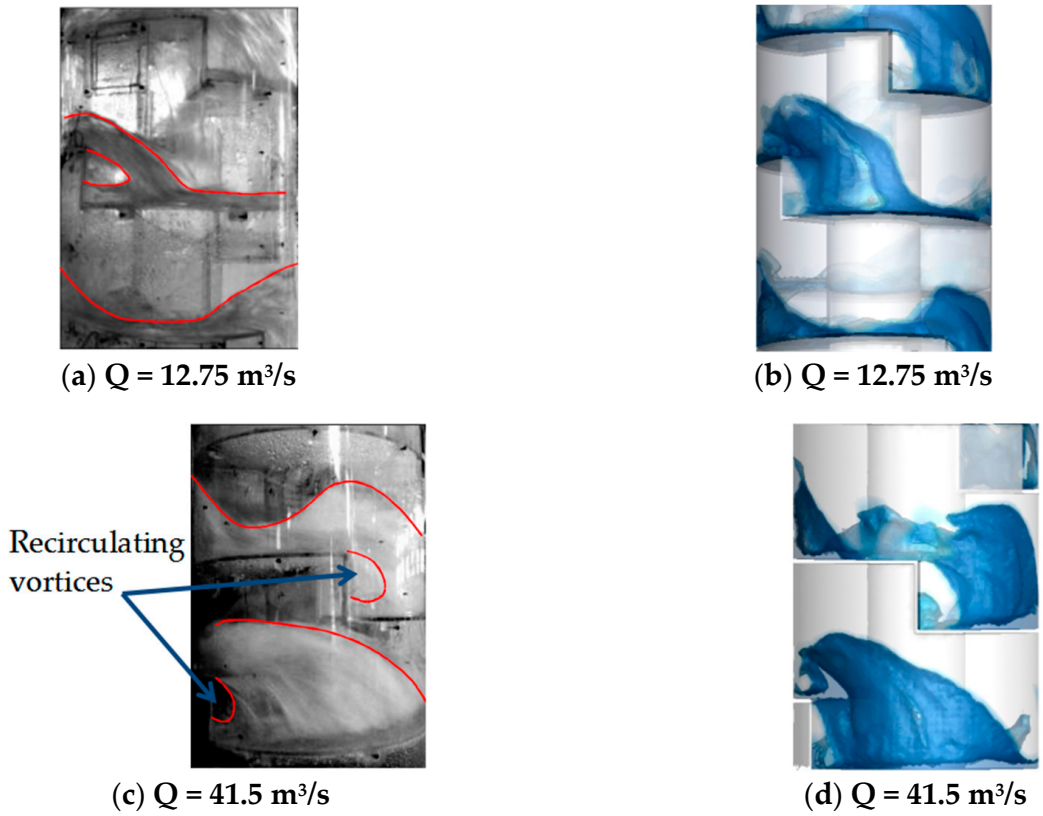

Figure 3. Comparison of experimental and calculated flow pattern: (**a**,**c**) flow pattern in experiment; (**b**,**d**) flow pattern in simulation.

In addition, experimental data obtained from Wu et al. [19] were used to verify the numerical results by comparing the stream-wise and radial pressure at S9, as is shown in Figure 4. In Figure 4a, four measuring points (P1~P4) were set on the center line of the bottom step along the flow direction. P3, and the other three measuring points (P5, P6, P7) were on a straight line that was paralleled to the y-axis in the radial direction. It can be seen from Figure 4b,c that, at most locations, the calculated results of pressure distribution were fairly consistent with that of laboratory tests. The maximums of the relative error for Q = 12.75 m^3/s and Q = 41.5 m^3/s were 7.5% and 10%, respectively, indicating that the numerical simulations produced reliable and acceptable results.

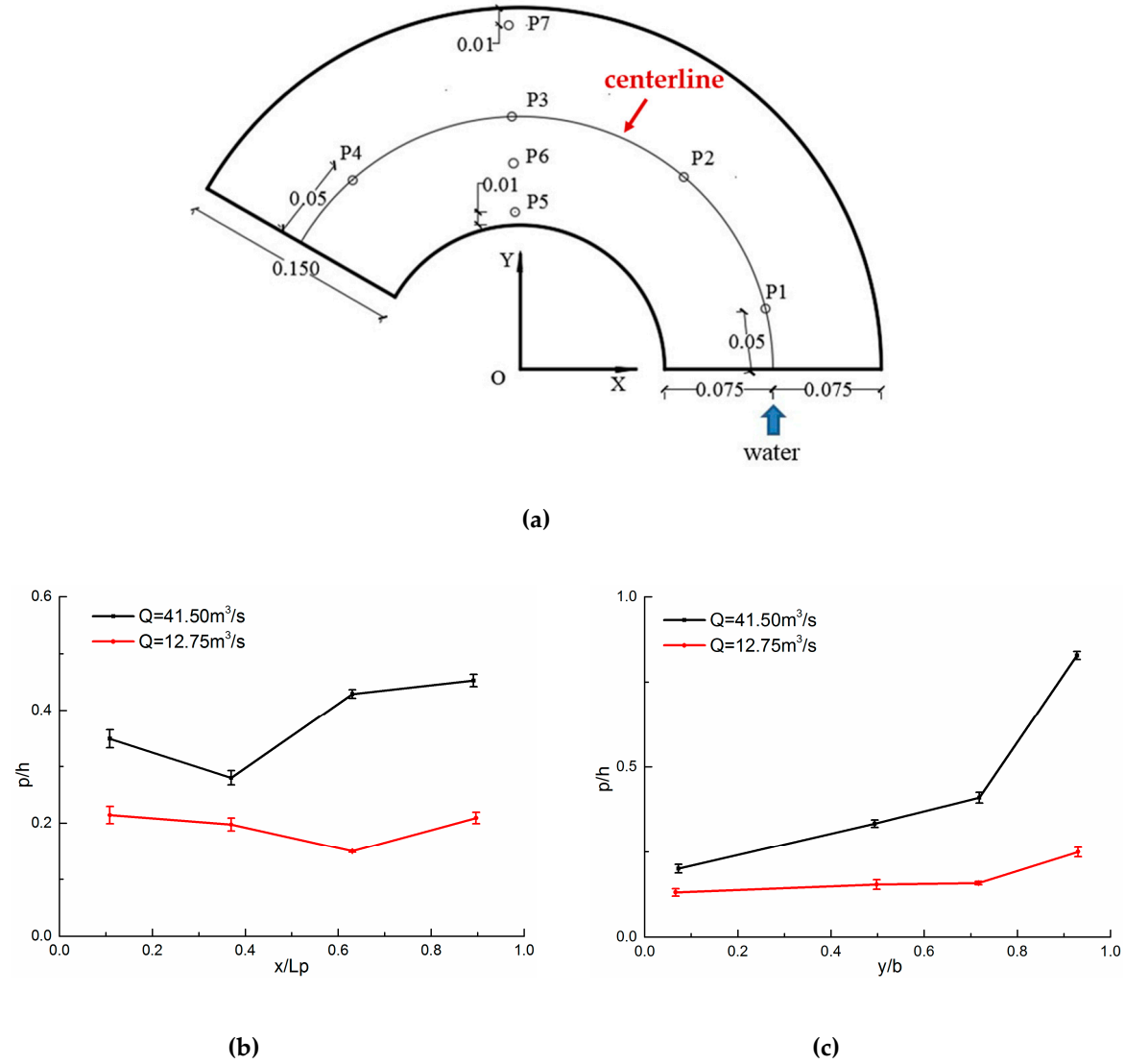

Figure 4. Comparison of numerical and experimental data: (**a**) location of the measuring points (m); (**b**) pressure distribution along the flow direction; (**c**) pressure distribution along the radical direction. Notes: L_p represents the arc length of the center line; b is the width of the horizontal step.

2.6.3. Fluctuation of Calculation Results

There existed instabilities and uncertainties in the computed results because of the complexity of the flow. In order to improve the reliability of results, the pressure for R = 0.25 m at S6 and the water surface on outer wall at S6 were monitored to analyze the fluctuation of pressure and water level in the calculation process. After a long time calculation, when the average relative errors of the mass flow rate were below 10%, the flow variables were considered relatively constant in this work. Five relative locations, namely, 10°, 30°, 60°, 90°, and 120°, were selected from each of the nine cases for determining the dispersion of pressure and the water surface at the same time period. The data in a duration of 10 s with an interval of 1 s were selected for analysis. The fluctuation of the data was calculated in terms of the standard deviation ($\sigma_{p/h}$ and $\sigma_{h_w/h}$). Table 2 shows the standard deviation of the variables for each case. In Table 2, the standard deviations of pressure and water surface were small, ranging from 0.0565 to 0.1008, indicating the reliability of the simulated results.

Table 2. Summary of the standard deviations of pressure and water surface in different locations at the same time period, where Er_{ave} represents the average relative errors of the mass flow rate of inlet and outlet; $\sigma_{p/h}$ and $\sigma_{h_w/h}$ are the standard deviation of pressure and water surface.

	Er_{ave} (%)		10°	30°	60°	90°	120°
case1	8.25	$\sigma_{p/h}$	0.0707	0.0692	0.0723	0.0818	0.0726
		$\sigma_{h_w/h}$	0.0852	0.0912	0.0823	0.0797	0.0906
case2	7.18	$\sigma_{p/h}$	0.0675	0.0704	0.0681	0.0619	0.0621
		$\sigma_{h_w/h}$	0.0823	0.0834	0.0885	0.0818	0.0911
case3	4.58	$\sigma_{p/h}$	0.0754	0.0652	0.0801	0.0781	0.0702
		$\sigma_{h_w/h}$	0.0925	0.0922	0.0879	0.0921	0.0942
case4	7.32	$\sigma_{p/h}$	0.0583	0.0621	0.0612	0.0565	0.0669
		$\sigma_{h_w/h}$	0.0725	0.0822	0.0850	0.0818	0.0861
case5	7.07	$\sigma_{p/h}$	0.0754	0.0689	0.0692	0.0717	0.0722
		$\sigma_{h_w/h}$	0.0628	0.0587	0.0603	0.0614	0.0592
case6	5.68	$\sigma_{p/h}$	0.0718	0.0782	0.0811	0.0777	0.0798
		$\sigma_{h_w/h}$	0.0823	0.0898	0.0912	0.0884	0.0879
case7	8.12	$\sigma_{p/h}$	0.0905	0.0972	0.0883	0.0878	0.0928
		$\sigma_{h_w/h}$	0.0923	0.0985	0.0984	0.1008	0.0954
case8	7.22	$\sigma_{p/h}$	0.0661	0.0622	0.0704	0.0683	0.0688
		$\sigma_{h_w/h}$	0.0921	0.0918	0.0856	0.0885	0.0892
case9	6.64	$\sigma_{p/h}$	0.0775	0.0721	0.0605	0.0644	0.0786
		$\sigma_{h_w/h}$	0.0858	0.0805	0.0734	0.0713	0.0728

All verifications for computational models, including the grid sensitivity study, the model verification, and the fluctuation of the calculated results, showed some errors and uncertainties due to the use of the eddy viscosity-based turbulence models. The errors of such eddy viscosity-based turbulence models in flow separation and recirculation zones have been documented in prior studies [45,46]. Nevertheless, using RNG k~ε to reveal the general flow patterns could satisfy the research requirements at the present stage.

3. Results and Analysis

3.1. Region Division in the Flow

As the simulation reveals, the flow transfers from one step to another, in which the flow regime has similar features on different steps. First, the successive impinging produces a bifurcation, where part of the flow moves backwards and forms a recirculation zone, while the main flow rotates along the sidewall with the vortex intensity decaying. Second, the flow undergoes a significant mixing and jumping process at the end of step. In order to present the complicated flow pattern of the stepped dropshaft accurately, the flow field is divided into the recirculating region (I), the wall-impinging region (II) and the mixing region (III), according to the flow characteristics. The relative ranges of these regions are expressed in terms of angles, namely, α_1, α_2, and α_3, respectively. In the subsequent sections, flow regions are discussed qualitatively according to individual streamlines and analyzed quantitatively on the basis of the pressure distribution for R = 0.25 m.

Figure 5 highlights the streamlines on the first step in each configuration. Although the central angle of each configuration was different, they shared similar flow features. In particular, the flow pattern had similar characteristics as well on other steps having the same central angle. Hence, only the flow on S6 in the different configuration under Q = 80 m^3/s was analyzed.

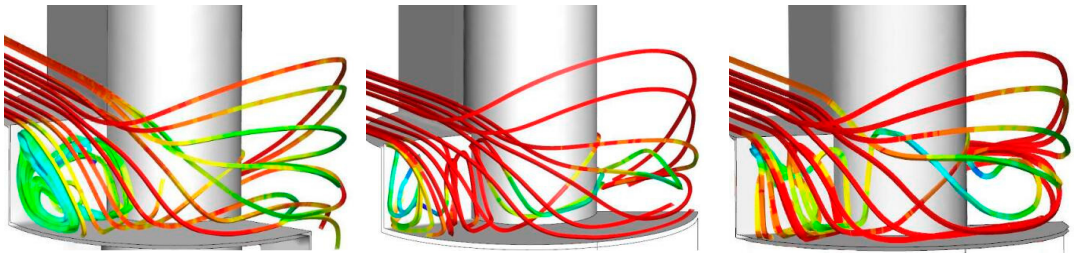

(**a**) (**b**) (**c**)

Figure 5. Streamlines above the S2 in different configurations: (**a**) 120°; (**b**) 150°; and (**c**) 180°.

(1) Recirculating region

The recirculating region was the zone where there was insignificant change of pressure gradient in the radial direction and streamline deflection in the opposite direction. Figure 6 illustrates the flow pattern along the flow direction in the cross-section for different configurations. Recirculating vortices can be found on the step due to the pressure difference between the upper and lower surfaces of the nappe flow during the falling process. Combined with the pressure difference and resistance caused by the nappe flow colliding with the horizontal step surface, the nappe flow departed from its original direction and formed a reflux. In addition, the location of recirculating moved from the external wall to the internal wall because of the curvature of the sidewall along the downstream direction. Figure 7 presents the pressure distributions on the horizontal step surfaces and the range of flow regimes. Most of the falling points were located at the intersection line of the horizontal step and the external wall. The most remarkable feature was that it was the minimum value of relative pressure that could be detected in the recirculating region.

(2) Wall-impinging region

The definition for wall-impinging region was the same as the recirculating region, which was mainly based on pressure variations and streamline features. Therefore, the range of the wall-impinging region was from the location where the minimum relative pressure occurred to the location where the local minimum pressure took place.

In the wall-impinging region, the flow was subjected to resistance and centrifugal force. However, the location and time that the inner and outer fluid were impacting the step or sidewall were different because of the curvature. First, the tangential velocity changed abruptly because of the impact of the surface flow near the external wall on that of the lateral one, leading it to increase rapidly and then to decline gradually on the water surface. The flow near the internal wall jetted along the tangent of that under pressure difference and gravity, and the maximum distance of the falling point of flow was in the circumferential direction, whereas the minimum was in the radial direction. For the lower level fluid, the flow quickly dived to the bottom of the step and traveled forward along the sidewall under the influence of gravity. However, the falling points of inside flow were close to the axis of the horizontal step surface. Deflected by the step, the flow deviated to the internal wall, resulting in it hitting the internal wall and attaching to it.

Therefore, the water surface was higher on the external wall than it was on the internal wall (Figure 5). Moreover, maximum pressure occurred and the pressure gradient showed drastic change at the start of the wall-impinging region (Figure 6).

(3) Mixing region

The range of the mixing region was from the location where the local minimum pressure occurred to the end of the step. The possibility of a relatively steady flow in the mixing region may be determined by the declining intensity of the swirling flow. The flow near the external wall moved inward from the bottom and the one close to the internal wall moved to the opposite from the surface due to the inward pressure gradient near the horizontal step which prevailed over the centrifugal force. As a result, there were less variations in the water surface in the transverse direction. Flow from the internal and the external walls mixed and interacted with each other near the axis of the step, causing the

fluctuation of water surface along the circumference. At the end of the step, the elevation of the water surface caused by the transverse gradient in the outer wall was higher than that in the inner wall. The pressure distribution in the mixing region exhibited no obvious change.

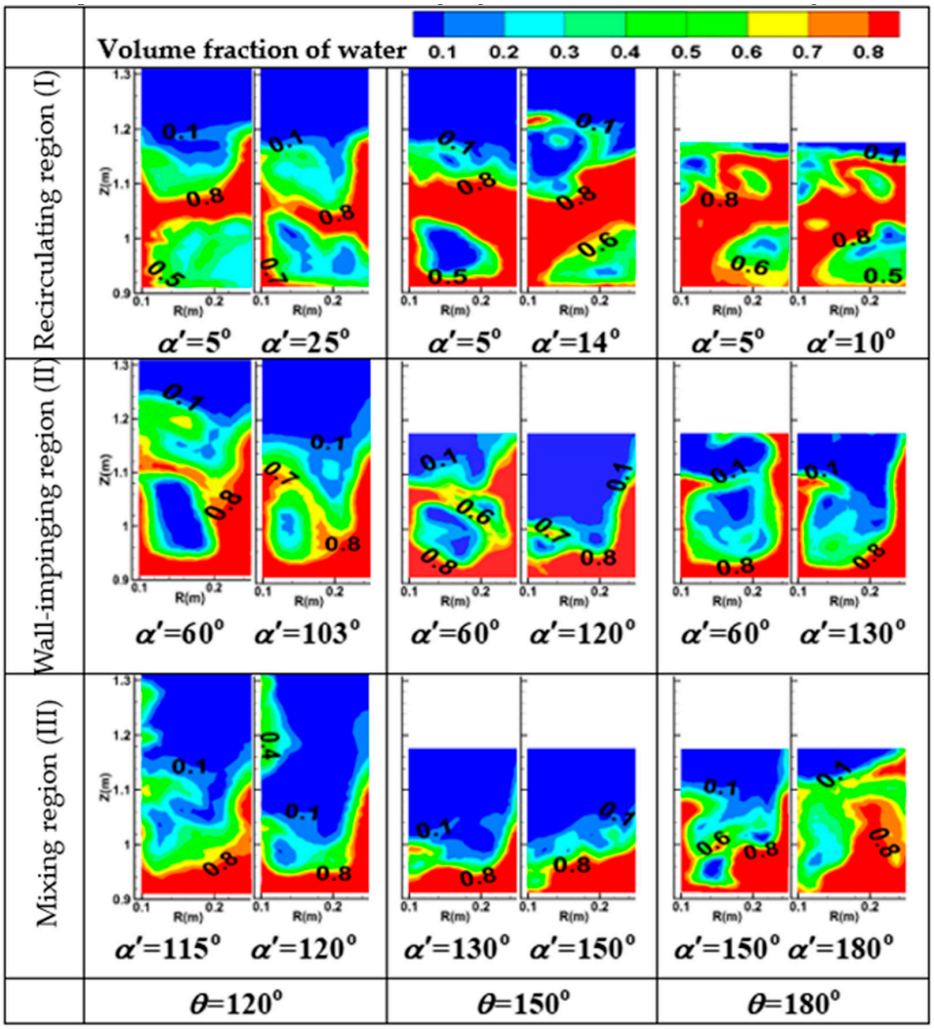

Figure 6. Flow pattern in the cross-section for different configurations, where α' is the relative location of the cross-section.

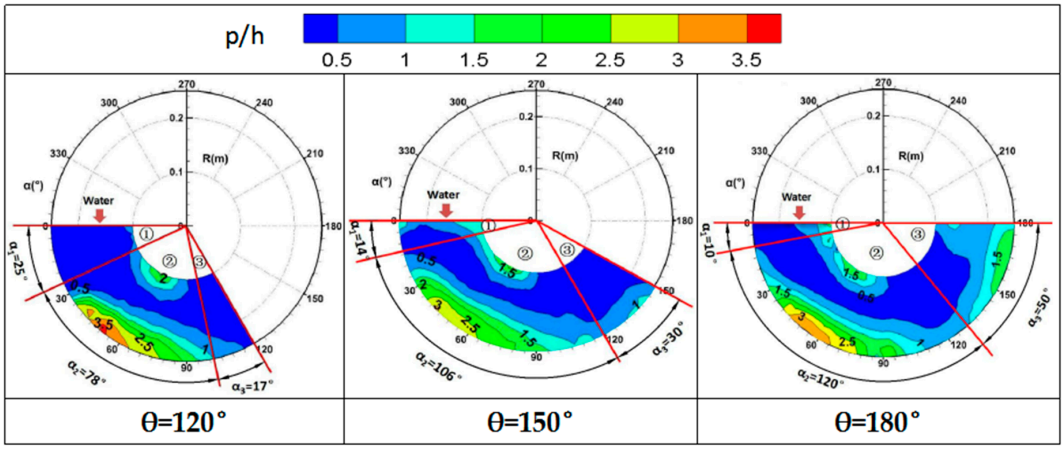

Figure 7. Pressure distribution and flow regions at S6.

3.2. Regional Scope

Figure 8 highlights the pressure distributions on the horizontal step for R = 0.25 m. As can be seen, the impact pressure fluctuated greatly with the maximum and minimum occurring in the recirculating region and the wall-impinging region, respectively, under all conditions. In addition, the pressure in the wall-impinging region showed greater gradient than that in the mixing region and the recirculating region. As the θ increased, α_1 decreased, while α_2 and α_3 increased. The cause of this phenomenon was attributed to the increase in the circumferential length of the step. These changes were able to bring the falling point of the jet flow to the vertical step closer and to make the recirculating region smaller. On the contrary, the ranges of the wall-impinging region and the mixing region were enhanced. Flow regime had little impact on the spectrum of flow regions in most cases with θ = 120° and θ = 150°, but a different phenomenon could be observed when θ = 180°. When flow discharge increased, α_2 increased, whereas α_3 decreased.

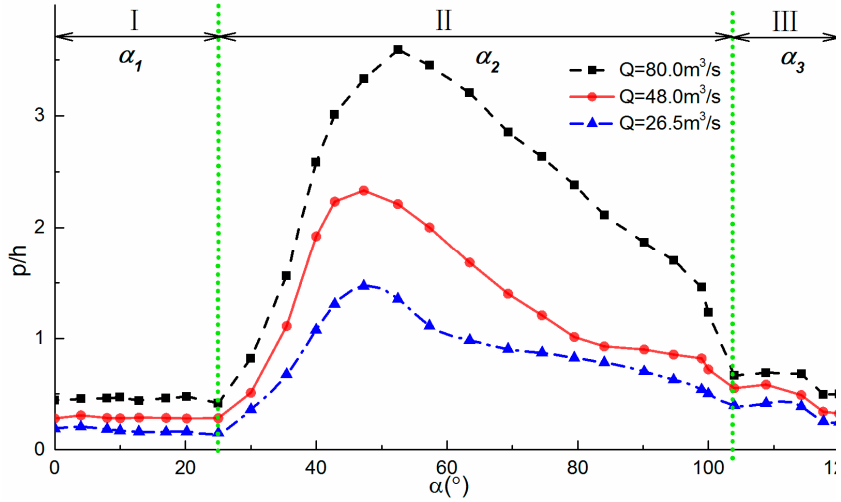

(**a**)

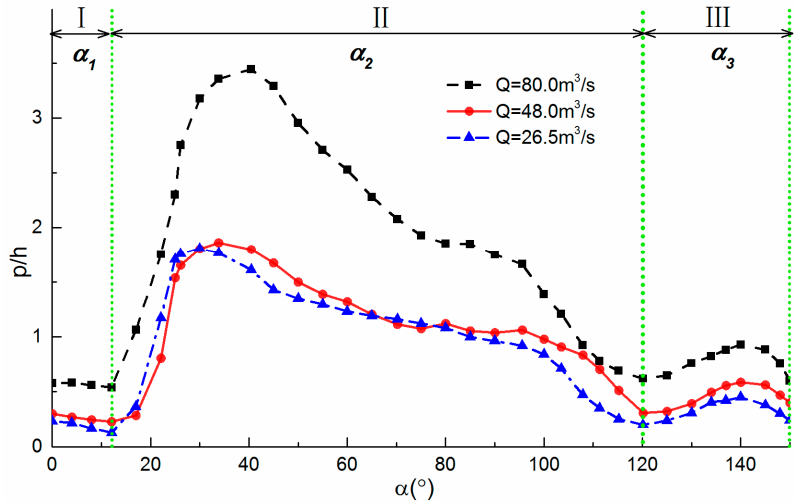

(**b**)

Figure 8. *Cont.*

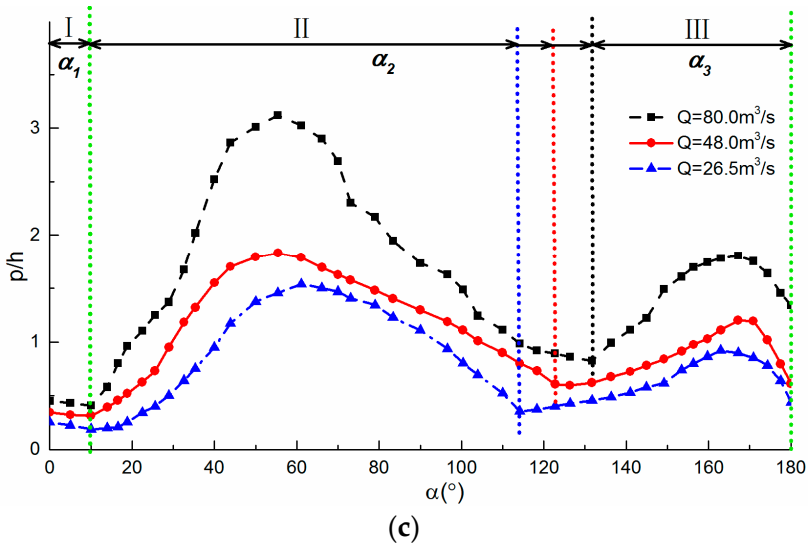

Figure 8. Pressure distribution for R = 0.25 m in different θ: (**a**) 120°; (**b**) 150°; and (**c**) 180°.

Figure 9a displays the average range of flow region on each step. Although some slight variations can be found, it is noticeable that the ranges of the regions were approximately the same under different flow conditions, indicating that the scope was mainly affected by the step angle rather than the flow regime. The chart compares the average range of different flow regions in all configurations.

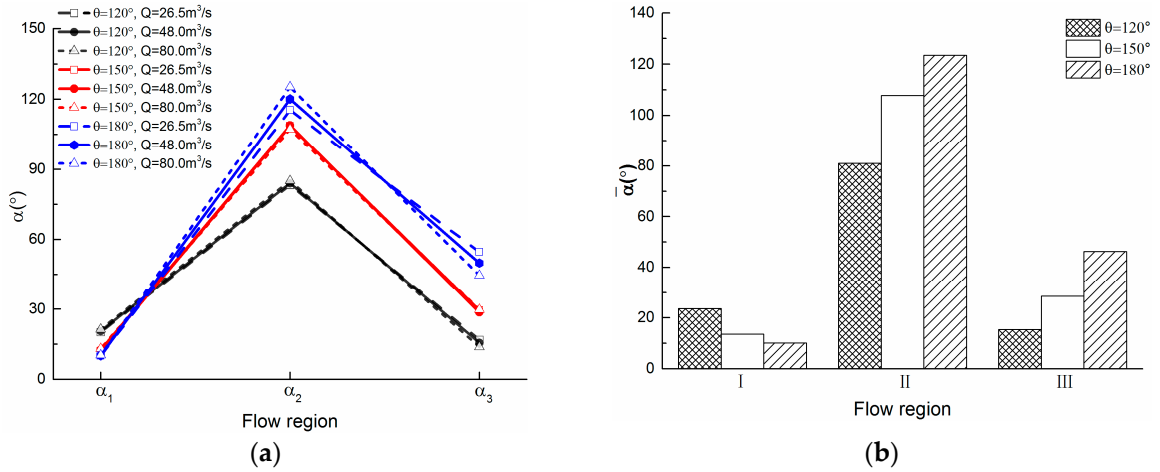

Figure 9. Flow region: (**a**) range of flow regions and (**b**) range of flow regions under different configurations.

3.3. Water Depth

For the traditional dropshaft, standing waves can only occur in a supercritical approach flow [47–49] channel due to sidewall deflection or curvature; therefore, the height of sidewalls must be carefully designed in a prototype environment. In addition, these standing waves can spread to downstream channels, causing fluctuations in the water surface. Nevertheless, for the dropshaft in the present work, sidewall standing waves were generated on each step, although the standing wave was quite insignificant under a small flow rate. Therefore, research studies should be undertaken to gain insights into the typical properties of standing waves. A sketch of the wave along the external wall is shown in Figure 10. h_{max} is the maximum water depth and α_{max} is the relative position of the maximum water depth. The distance between the steps is h_s, and the relative position of the vertical plane of the upper step is α_s. A dimensionless height, h_s/h, for θ = 120° and θ = 180° is, respectively,

3 and 2, and the location, α_s, for both $\theta = 120°$ and $\theta = 180°$ is 0. However, for $\theta = 150°$, h_s/h and α_s vary significantly with h_s/h ranging from 3 to 2 and α_s ranging from 0° to 60°.

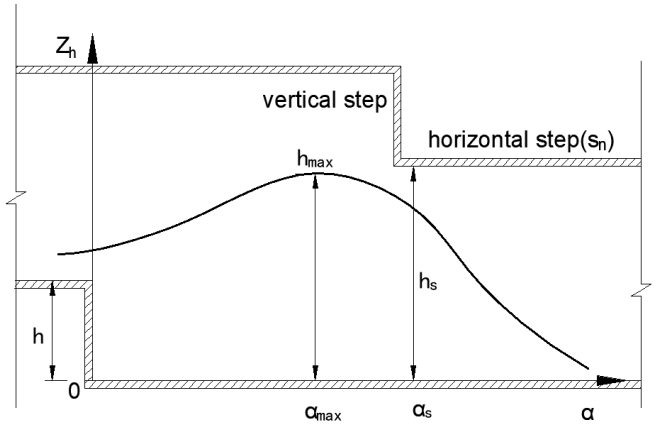

Figure 10. Water depth along the external wall.

Figure 11 demonstrates the flow profile along the external wall. The flow-depth curves indicated that the water surface along the outer wall presented a similar wavy pattern under different conditions.

(1) With the increase in the central angles of step, drastic fluctuation began to occur. For $\theta = 120°$, the water-surface profile was steady and the water depth decreased gradually along the flow direction in which the maximum relative water depth occurred in the recirculating region. For $\theta = 150°$, the variation of free surface became remarkable. When the central angle of step increased to 180°, the oscillation of water surface was more violent than that of the other cases.

For the small center angle, as the rotational flow approached the mixing region, the flow fell into the next step suddenly owing to the small range of the mixing region, which could lead to a dramatic change in axial velocity gradient and water depth. However, the larger the angle, the greater the diffusion in the mixing region. Water surface fluctuated greatly due to the resistance of the sidewall and centrifugal force.

(2) The influence of flow rate on water depth was relatively noteworthy: the water level rose with the increase in discharge under different conditions. For $\theta = 120°$ and $\theta = 150°$, the free surface changed without distinct oscillation under all circumstances. For $\theta = 180°$, the water level oscillated more vigorously with a further increase in discharge, causing an increase in the water surface, and hit the vertical surface of the next step in the mixing region.

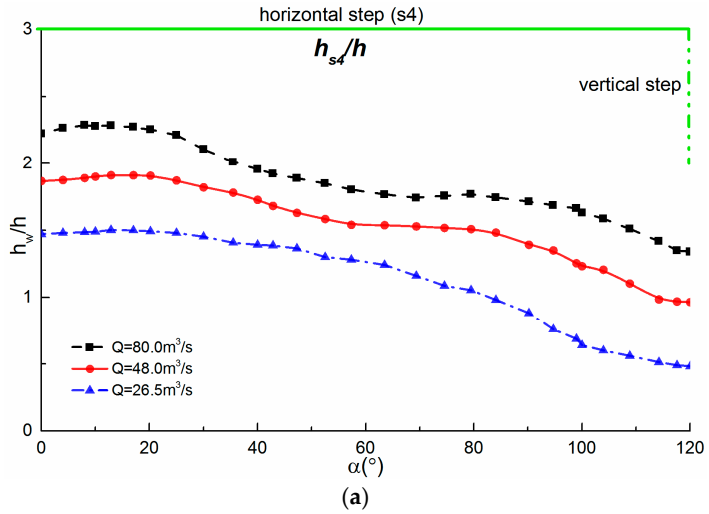

(**a**)

Figure 11. *Cont.*

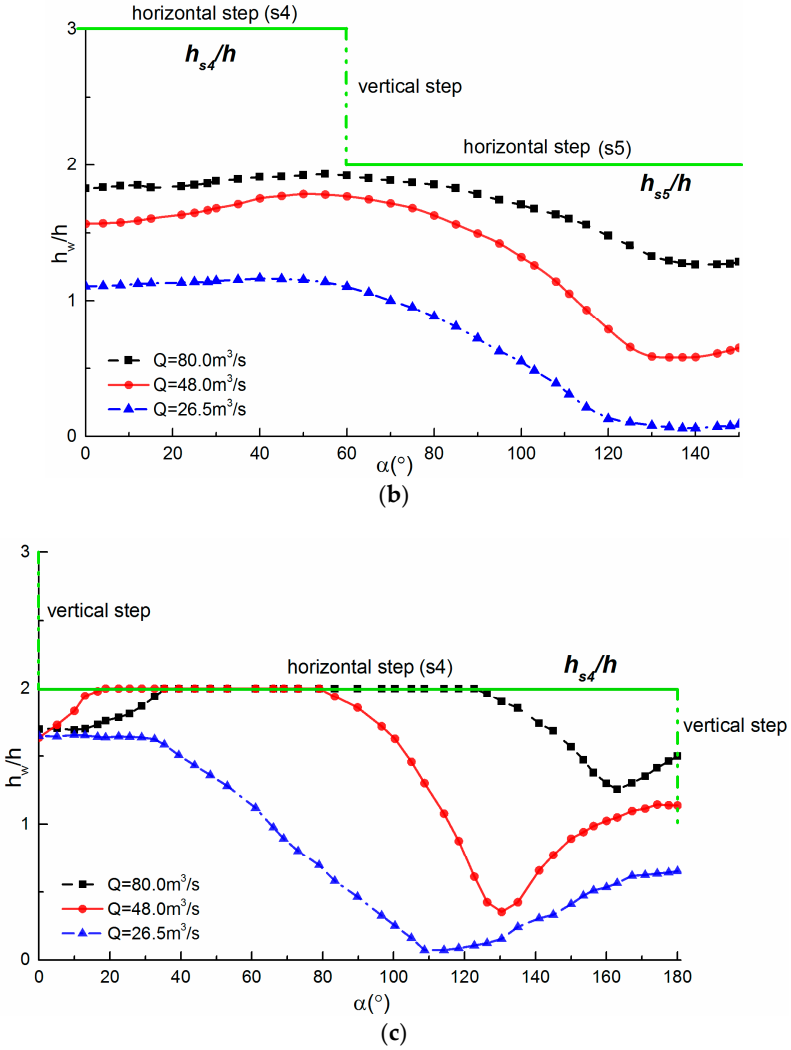

Figure 11. Water surface curves: (**a**) 120°; (**b**) 150°; and (**c**) 180°.

Figure 12 illustrates the change of relative maximum water depth in all cases and yields the following conclusions:

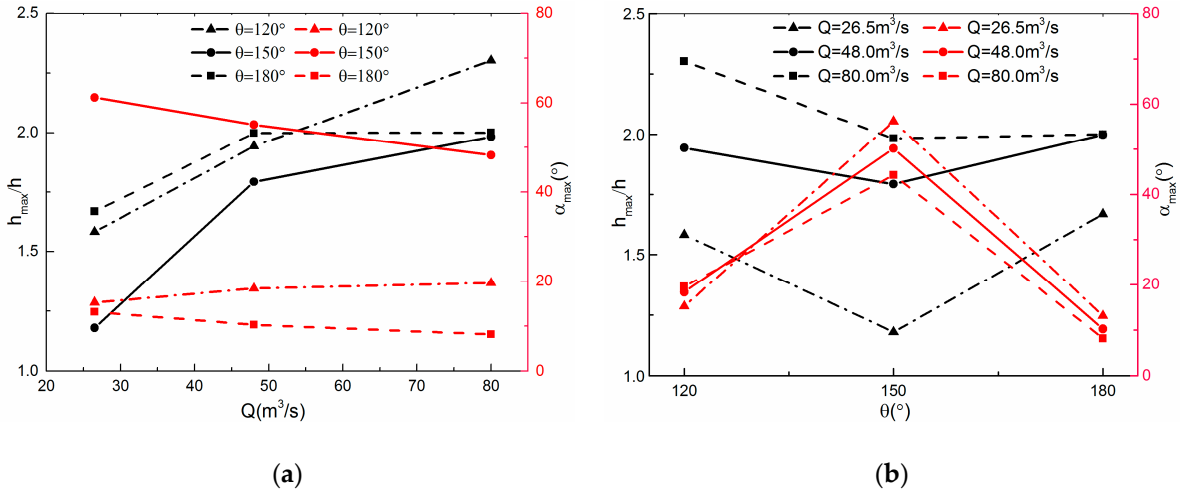

Figure 12. Water depth characteristics: (**a**) the relationship between $h_{\max}/h$, $\alpha_{\max}$ and Q and (**b**) the relationship between $h_{\max}/h$, $\alpha_{\max}$ and θ.

(1) For a fixed central angle of step θ, h_{max}/h and α_{max} increased as Q increased.

(2) For a fixed discharge Q, h_{max}/h and α_{max} showed no obvious trend as θ increased.

(3) With the increment of θ, h_{max}/h decreased initially and then increased, whereas α_{max} exhibited the opposite phenomenon.

(4) With the increase in Q, h_{max}/h increased and α_{max} presented no evident change.

Therefore, it seemed that the range of h_{max}/h depended on the discharge and the central angle of step, whereas the range of α_{max} was associated with the central angle of step. For $\theta = 180°$, when $h_{max}/h = 2$ ($Q = 48$ m^3/s, 80 m^3/s), the flow impacted the bottom of the upper step, which can only occur on some steps when $\theta = 150°$ for $Q = 80$ m^3/s. For $\theta = 120°$, h_{max}/h was considerably lower than the height of the upper step in all discharge.

4. Conclusions

For all the cases considered above in this paper, the RNG k~ε turbulence flow model is capable of predicting the main characteristics of the flow. This included the definition of the flow regime and the determination of the maximum water depth. The following conclusions can be drawn:

1. Because of the complexity of the flow regime, the flow was partitioned into the recirculating region, the wall-impinging region, and the mixing region.

2. The range of the three regions was affected by the central angle of step. With the increase in θ, the range of the wall-impinging region and the mixing region increased, whereas the range of the recirculating region had no significant change.

3. The maximum water depth increased with the increase in the flow rate, whereas the flow rate showed little effect on α_{max}. Moreover, with the increase in θ, the maximum water depth initially decreased and then increased; however, α_{max} displayed the opposite trend.

Although the results of this study are encouraging, same solution processes can be adopted in future work to model the energy dissipation performance and air entertainment characteristics of stepped dropshafts.

Author Contributions: Conceptualization and Methodology, Y.W. and J.Z.; Numerical Simulation, Y.Q.; Investigation, Y.Q.; Writing—Original Draft Preparation, Y.Q.; Writing—Review and Editing, Y.W. and J.Z.; Supervision, Y.W. and J.Z.; Project Administration, Y.W. and J.Z.; Funding Acquisition, Y.W. and J.Z.

Funding: This research was funded by the National Key Research and Development Program of China (No. 2016YFC0401707), the National Natural Science Foundation of China (No. 51579165), and the National Science Fund for Distinguished Young Scholars (No. 51625901).

Conflicts of Interest: The authors declare no conflict of interest.

References

1. Rajaratnam, N.; Mainali, A.; Hsung, C. Observations on flow in vertical dropshafts in urban drainage systems. *J. Environ. Eng.* **1997**, *123*, 486–491. [CrossRef]
2. Chanson, H. Hydraulics of rectangular dropshafts. *J. Irrig. Drain. Eng.* **2004**, *130*, 523–529. [CrossRef]
3. Chanson, H. Understanding air–water mass transfer in rectangular dropshafts. *J. Environ. Eng. Sci.* **2004**, *3*, 319–330. [CrossRef]
4. Adriana Camino, G.; Zhu, D.Z.; Rajaratnam, N. Flow observations in tall plunging flow dropshafts. *J. Hydraul. Eng.* **2014**, *141*, 06014020. [CrossRef]
5. Granata, F.; de Marinis, G.; Gargano, R.; Hager, W.H. Hydraulics of circular drop manholes. *J. Irrig. Drain. Eng.* **2010**, *137*, 102–111. [CrossRef]
6. Ma, Y.; Zhu, D.Z.; Rajaratnam, N.; van Duin, B. Energy dissipation in circular drop manholes. *J. Irrig. Drain. Eng.* **2017**, *143*, 04017047. [CrossRef]
7. Jain, S.C. Air transport in vortex-flow drop shafts. *J. Hydraul. Eng.* **1988**, *114*, 1485–1497. [CrossRef]
8. Vischer, D.; Hager, W. Vortex drops. In *Energy Dissipators*; Routledge: Abingdon, UK, 2018; pp. 167–181. ISBN 9781351451345.

9. Odgaard, A.J.; Lyons, T.C.; Craig, A.J. Baffle-drop structure design relationships. *J. Hydraul. Eng.* **2013**, *139*, 995–1002. [CrossRef]
10. Stirrup, M.; Margevicius, T.; Hrkac, T.; Baca, A. A baffling solution to Sewage Conveyance In York Region, Ontario. *Proc. Water Environ. Fed.* **2012**, *2012*, 74–90. [CrossRef]
11. Kennedy, J.F.; Jain, S.C.; Quinones, R.R. Helicoidal-ramp dropshaft. *J. Hydraul. Eng.* **1988**, *114*, 315–325. [CrossRef]
12. Tamura, S.; Matsushima, O.; Yoshikawa, S. Helicoidal-ramp type drop shaft to deal with high head drop works in manholes. *Proc. Water Environ. Fed.* **2010**, *2010*, 4991–5002. [CrossRef]
13. Jain, S.C.; Kennedy, J.F. *Vortex-Flow Drop Structures for the Milwaukee Metropolitan Sewerage District Inline Storage System*; Iowa Institute of Hydraulic Research, The University of Iowa: Iowa City, IA, USA, 1983.
14. Hager, W.H. *Wastewater Hydraulics: Theory and Practice*; Springer Science & Business Media: Berlin, Germany, 2010.
15. Zhao, C.H.; Zhu, D.Z.; Sun, S.K.; Liu, Z.P. Experimental study of flow in a vortex drop shaft. *J. Hydraul. Eng.* **2006**, *132*, 61–68. [CrossRef]
16. Del Giudice, G.; Gisonni, C. Vortex dropshaft retrofitting: Case of Naples city (Italy). *J. Hydraul. Res.* **2011**, *49*, 804–808. [CrossRef]
17. Natarius, E.M. Aeration performance of vortex flow insert assemblies in sewer drop structures. *Proc. Water Environ. Fed.* **2008**, *2008*, 842–851. [CrossRef]
18. Yu, D.; Lee, J.H. Hydraulics of tangential vortex intake for urban drainage. *J. Hydraul. Eng.* **2009**, *135*, 164–174. [CrossRef]
19. Wu, J.H.; Yang, T.; Sheng, J.Y.; Ren, W.C.; Fei, M.A. Hydraulic characteristics of stepped spillway dropshafts with large angle. *Chin. J. Hydrodyn.* **2018**, *33*, 176–180. (In Chinese) [CrossRef]
20. Christodoulou, G.C. Energy dissipation on stepped spillways. *J. Hydraul. Eng.* **1993**, *119*, 644–650. [CrossRef]
21. Sorensen, R.M. Stepped spillway hydraulic model investigation. *J. Hydraul. Eng.* **1985**, *111*, 1461–1472. [CrossRef]
22. Frizell, K.W.; Renna, F.M.; Matos, J. Cavitation potential of flow on stepped spillways. *J. Hydraul. Eng.* **2012**, *139*, 630–636. [CrossRef]
23. Wu, J.H.; Ren, W.C.; Ma, F. Standing wave at dropshaft inlets. *J. Hydrodyn. Ser. B* **2017**, *29*, 524–527. [CrossRef]
24. Hirt, C.W.; Nichols, B.D. Volume of fluid (VOF) method for the dynamics of free boundaries. *J. Comput. Phys.* **1981**, *39*, 201–225. [CrossRef]
25. Peng, Y.; Zhou, J.G.; Burrows, R. Modelling the free surface flow in rectangular shallow basins by lattice Boltzmann method. *J. Hydrau. Eng.* **2011**, *137*, 1680–1685. [CrossRef]
26. Peng, Y.; Zhou, J.G.; Burrows, R. Modelling solute transport in shallow water with the lattice Boltzmann method. *Comput. Fluids.* **2011**, *50*, 181–188. [CrossRef]
27. Peng, Y.; Zhang, J.M.; Zhou, J.G. Lattice Boltzmann Model Using Two-Relaxation-Time for Shallow Water Equations. *J. Hydrau. Eng.* **2016**, *142*, 06015017. [CrossRef]
28. Peng, Y.; Zhang, J.M.; Meng, J.P. Second order force scheme for lattice Boltzmann model of shallow water flows. *J. Hydraul. Res.* **2017**, *55*, 592–597. [CrossRef]
29. Peng, Y.; Mao, Y.F.; Wang, B.; Xie, B. Study on C-S and P-R EOS in pseudo-potential lattice Boltzmann model for two-phase flows. *Int. J. Mod. Phys. C* **2017**, *28*, 1750120. [CrossRef]
30. Peng, Y.; Wang, B.; Mao, Y.F. Study on force schemes in pseudopotential lattice Boltzmann model for two-phase flows. *Math. Probl. Eng.* **2018**. [CrossRef]
31. Galván, S.; Reggio, M.; Guibault, F. Assessment study of k-ε turbulence models and near-wall modeling for steady state swirling flow analysis in draft tube using fluent. *Eng. Appl. Comput. Fluid* **2011**, *5*, 459–478. [CrossRef]
32. Morovati, K.; Eghbalzadeh, A.; Javan, M. Numerical investigation of the configuration of the pools on the flow pattern passing over pooled stepped spillway in skimming flow regime. *Acta Mech.* **2015**, *227*, 1–14. [CrossRef]
33. Devolder, B.; Troch, P.; Rauwoens, P. Performance of a buoyancy-modified k-ω and k-ω SST turbulence model for simulating wave breaking under regular waves using OpenFOAM®. *Coast. Eng.* **2018**, *138*, 49–65. [CrossRef]
34. Fuhrman, D.R.; Dixen, M.; Jacobsen, N.G. Physically-consistent wall boundary conditions for the k-ω turbulence model. *J. Hydraul. Res.* **2010**, *48*, 793–800. [CrossRef]

35. Bai, Z.L.; Zhang, J.M. Comparison of different turbulence models for numerical simulation of pressure distribution in V-shaped stepped spillway. *Math. Probl. Eng.* **2017**, *2017*, 1–9. [CrossRef]
36. Li, S.; Zhang, J. Numerical investigation on the hydraulic properties of the skimming flow over pooled stepped spillway. *Water* **2018**, *10*, 1478. [CrossRef]
37. Chan, S.; Qiao, Q.; Lee, J.H. On the three-dimensional flow of a stable tangential vortex intake. *J. Hydro-Environ. Res.* **2018**, *21*, 29–42. [CrossRef]
38. Gao, X.P.; Zhang, H.; Liu, J.J.; Sun, B.; Tian, Y. Numerical investigation of flow in a vertical pipe inlet/outlet with a horizontal anti-vortex plate: Effect of diversion orifices height and divergence angle. *Eng. Appl. Comput. Fluid Mech.* **2018**, *12*, 182–194. [CrossRef]
39. Yakhot, V.; Orszag, S.A. Renormalization group analysis of turbulence. I. Basic theory. *J. Sci. Comput.* **1986**, *57*, 1722. [CrossRef]
40. Liu, Z.P.; Guo, X.L.; Xia, Q.F.; Fu, H.; Wang, T.; Dong, X.L. Experimental and numerical investigation of flow in a newly developed vortex drop shaft spillway. *J. Hydraul. Eng.* **2018**, *144*, 04018014. [CrossRef]
41. Zhang, W.; Wang, J.; Zhou, C.; Dong, Z.; Zhou, Z. Numerical simulation of hydraulic characteristics in a vortex drop shaft. *Water* **2018**, *10*, 1393. [CrossRef]
42. Guo, X.L.; Xia, Q.F.; Fu, H.; Yang, K.L.; Li, S.J. Numerical study on flow of newly vortex drop shaft spillway. *J. Hydraul. Eng.* **2016**, *47*, 733–741. (In Chinese) [CrossRef]
43. *ANSYS Fluent Theory Guide*; Release 16.0; ANSYS Inc.: Canonsburg, PA, USA, 2015.
44. Celik, I.B.; Ghia, U.; Roache, P.J. Procedure for estimation and reporting of uncertainty due to discretization in CFD applications. *J. Fluids Eng.* **2008**, *130*. [CrossRef]
45. Iaccarino, G.; Mishra, A.A.; Ghili, S. Eigenspace perturbations for uncertainty estimation of single-point turbulence closures. *Phys. Rev. Fluids* **2017**, *2*, 024605. [CrossRef]
46. Mishra, A.A.; Iaccarino, G. Uncertainty Estimation for Reynolds-Averaged Navier–Stokes Predictions of High-Speed Aircraft Nozzle Jets. *AIAA J.* **2017**, 3999–4004. [CrossRef]
47. Del Giudice, G.; Gisonni, C.; Rasulo, G. Design of a scroll vortex inlet for supercritical approach flow. *J. Hydraul. Eng.* **2010**, *136*, 837–841. [CrossRef]
48. Hager, W.H. Vortex drop inlet for supercritical approaching flow. *J. Hydraul. Eng.* **1990**, *116*, 1048–1054. [CrossRef]
49. Kawagoshi, N.; Hager, W. Wave type flow at abrupt drops Wave type flow at abrupt drops: I. Flow geometry. *J. Hydraul. Res.* **1990**, *28*, 235–252. [CrossRef]